Eur. Phys. J. A **23**, 135–146 (2005)
DOI 10.1140/epja/i2004-10057-1

THE EUROPEAN PHYSICAL JOURNAL A

The neutron decay retardation spectrometer aSPECT: Electromagnetic design and systematic effects

F. Glück[1,2,3,a], S. Baeßler[1], J. Byrne[4], M.G.D. van der Grinten[4], F.J. Hartmann[5], W. Heil[1], I. Konorov[5], G. Petzoldt[5], Yu. Sobolev[1], and O. Zimmer[5]

[1] Institut für Physik, Universität Mainz, D-55099 Mainz, Germany
[2] Research Institute for Nuclear and Particle Physics, Theory Department P.O. Box 49, H-1525 Budapest 114, Hungary
[3] Institut für Kernphysik, Forschungszentrum Karlsruhe, Pf. 3640, D-76021 Karlsruhe, Germany
[4] Department of Physics and Astronomy, University of Sussex, Falmer, Brighton, BN1 9QH, UK
[5] Physik-Department E18, Technische Universität München, D-85748 Garching, Germany

Received: 2 February 2004 / Revised version: 7 July 2004 /
Published online: 23 November 2004 –
Communicated by Th. Walcher

Abstract. The apparatus described here, *a*SPECT, will be used for a measurement of the neutrino-electron angular correlation coefficient a in the decay of free neutrons. The idea of the *a*SPECT spectrometer is to measure the integrated proton energy spectrum very accurately using an energy filter by electrostatic retardation and magnetic adiabatic collimation. The main ideas of the spectrometer are presented, followed by an explanation of the adiabatic transmission function. Details of the superconducting coil and of the electrode system are given, as well as a discussion of the most important systematic effects: magnetic field and electrostatic potential inhomogeneities, deviation from adiabatic motion, scattering in the residual gas, background, Doppler effect, edge effect, and detector efficiency. Using this spectrometer, the parameter a is planned to be measured with an absolute experimental uncertainty of $\delta a \approx 3 \cdot 10^{-4}$, from which the axial vector to vector coupling constant ratio λ can be determined with an accuracy of $\delta\lambda \approx 0.001$.

PACS. 23.40.-s Beta decay; double beta decay; electron and muon capture – 13.30.-a Decays of baryons – 12.15.Hh Determination of Kobayashi-Maskawa matrix elements

1 Introduction

Free-neutron-decay experiments provide a sensitive tool for a reliable determination of various important parameters of the Standard Model (SM) of particle physics. Being a mixed superallowed weak transition with accurately known Fermi and Gamow-Teller matrix elements, one can determine the weak vector and axial vector coupling constants $G_{\rm V}$ and $G_{\rm A}$. Two independent measurements are required, *e.g.* the neutron lifetime together with an observable sensitive to the ratio $\lambda = G_{\rm A}/G_{\rm V}$. The importance of these values for applications in astrophysics, big bang cosmology, solar physics and for calculating hadronic weak-interaction cross-sections, *e.g.* for neutrino detection, has long been recognized (see the reviews [1–3] and references therein). From a more fundamental viewpoint, the value of $G_{\rm V}$, compared with its purely leptonic counterpart obtained from muon decay, provides a value for the element $V_{\rm ud}$ of the Cabibbo-Kobayashi-Maskawa (CKM) quark-mixing matrix. Including the experimental values of the elements $V_{\rm us}$ and $V_{\rm ub}$ from strange and B-meson decays results in a sensitive test of CKM unitarity [4]. Secondly, the ratio $\lambda = G_{\rm A}/G_{\rm V}$ may illuminate the role of the hadronic environment to the fundamental interactions among first generation quarks [5]. However, the present accuracy of theoretical predictions of λ is still low compared to experimental uncertainties, and therefore quark model calculations and the Cabibbo model use λ rather as an input value.

Due to the absence of nuclear structure effects, λ can be deduced much more accurately from neutron decay than from any other beta decay. The theoretical analysis of neutron decay is relatively simple, because of the near absence of uncertainties caused by model-dependent strong-interaction effects. In addition, the absence of competitive decay modes is an important experimental advantage. Neutron decay offers several alternative possibilities to measure λ, and the different observables have different sensitivities to non-SM physics. Therefore, the comparison of values of λ obtained by alternative means provides a test of the structure of the charged-current weak interaction at low energy. Important constraints follow for the

[a] e-mail: Ferenc.Glueck@ik.fzk.de

weak right-handed vector and axial vector couplings, as well as for left-handed and right-handed scalar and tensor couplings [6–8].

Two important possibilities for the determination of λ in neutron decay are the measurements of the beta asymmetry parameter A and of the neutrino-electron angular correlation coefficient a. Thus far, the beta asymmetry measurements [9–11] have provided the best results, which we denote by λ_A. The most recent and accurate result of an individual experiment, $\lambda_A = -1.2740 \pm 0.0021$, was measured with the spectrometer PERKEO II, leading to an about 3σ deviation from CKM unitarity [11]. A similar unitarity anomaly has long been present in superallowed Fermi beta decays [12] (although this anomaly is not without dispute [13]). On the other hand, the PERKEO II result disagrees with the results of the former determinations of A (see [14]).

To clarify the situation, one should focus on an alternative observable, which has entirely different systematic uncertainties. An accurate measurement of the coefficient a would therefore be very valuable. In beta decay of unpolarized neutrons the differential transition probability $\mathrm{d}W$ for fixed (total relativistic) electron energy E_e is

$$\mathrm{d}W \propto 1 + b\frac{m_\mathrm{e}}{E_\mathrm{e}} + a\beta\cos\theta_{\mathrm{e}\nu}, \qquad (1)$$

where b is the Fierz parameter, β is the electron velocity in units of the velocity of light, m_e is the electron mass, and $\theta_{\mathrm{e}\nu}$ is the angle between the directions of the electron and the antineutrino (in this expression, recoil order terms and radiative corrections are neglected). In the Standard Model, $b = 0$, and the λ-dependence of the coefficient a is given by

$$a = \frac{1-\lambda^2}{1+3\lambda^2}, \qquad \lambda = \frac{G_\mathrm{A}}{G_\mathrm{V}}. \qquad (2)$$

Denoting the experimental value of λ derived from this equation by λ_a, the goal must be to deduce it with at least the same accuracy as λ_A. The present best value, $\lambda_a = -1.263 \pm 0.013$, corresponding to $a = -0.1029$, is the average of the measurements published in refs. [15,16]. Obviously, the accuracy is still insufficient for a meaningful comparison to be made between the values of λ_A and λ_a; the accuracy of a needs to be improved by at least one order of magnitude.

There are various methods for determining a from experiments, where electrons and protons are detected in coincidence [1]. Unfortunately, this approach strongly depends on the precision of the electron energy measurements. However, as imposed by energy and momentum conservation, a can also be determined via the proton energy spectrum, without involving any electron detection. To reach the required high sensitivity, we are developing the new retardation spectrometer aSPECT, which was proposed in ref. [17]. After a brief review of the basic ideas, the present paper will describe the concrete design of the electromagnetic field configuration, and provide additional details in the discussion of systematic effects.

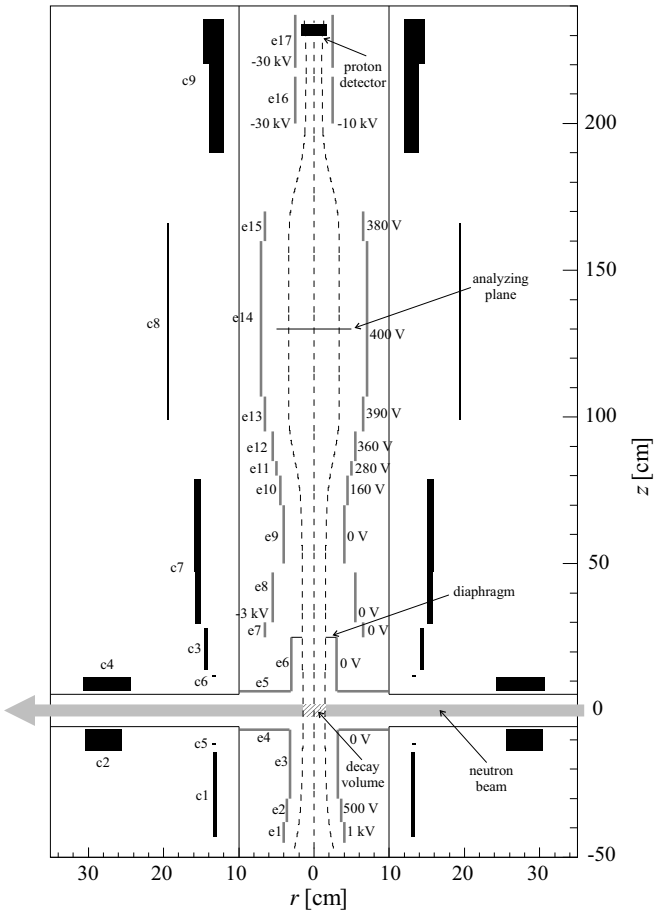

Fig. 1. A sketch of the spectrometer aSPECT. The coils are denoted by c1-c9, the dashed lines indicate magnetic field lines. The electrodes are denoted by e1-e17, and potential settings are given exemplary for $U_\mathrm{A} - U_0 = 400\,\mathrm{V}$ (note that two values are given for each of the two dipole electrodes e8 and e16).

2 The retardation spectrometer aSPECT

Figure 1 shows the system of the coils and the electrodes of the spectrometer. The neutron beam passes through the region with a strong magnetic field. Decay protons with an initial momentum component in the direction of the proton detector are guided towards the detector by the magnetic field lines. In the intermediate region with a weaker magnetic field, the central cylindrical electrode e14 generates the electrostatic potential barrier; the maximum of the electric potential is at the analyzing plane. Protons emitted in the hemisphere opposite to the detector are reflected back by the electrostatic mirror electrode e1 held at a potential larger than the maximum proton kinetic energy ($\approx 750\,\mathrm{eV}$). The spectrometer thus has 4π acceptance for protons which are created in the decay volume. Protons with sufficiently high energy can pass the barrier and will be accelerated towards a proton detector held at a high negative voltage (about $-30\,\mathrm{kV}$). We can measure the integrated spectrum of the protons using different settings of the barrier potential.

The motion of a charged particle in a spatially slowly varying magnetic field can be split in a first approximation into a gyration around a magnetic field line and a linear motion along this field line. Protons moving into the low field region have to keep their orbital magnetic moment constant, provided the magnetic-field change is slow enough that the motion is adiabatic [18]. Since also energy has to be conserved, an increase of their longitudinal momentum is required, while the energy in the gyration is decreased in the low-field region. This process is called inverse magnetic mirror effect or magnetic adiabatic collimation. In the design of *a*SPECT, the magnetic field B_0 in the decay volume is larger by a factor 5 than the field B_A in the analyzing plane.

The action of the potential barrier can be described by a transmission function, which is the probability that a proton with a definite starting kinetic energy passes the analyzing plane. An accurate knowledge of the transmission function is essential, which can be guaranteed by keeping the motion of the decay protons adiabatic. In this case, the transmission function can be expressed analytically. It depends only on the electrostatic potential and magnetic field values in the decay volume and in the analyzing plane. It does neither depend on the fields in between, nor on geometrical parameters. Furthermore, it does not depend on the detector characteristics, as long as the detector just counts the protons which pass the analyzing plane. In reality, deviations from the ideal behaviour have to be taken into account. These issues will be discussed below.

The principle of magnetic adiabatic collimation was first applied in electron spectroscopy [19]. Starting in the mid-eighties, this principle was successfully employed at Troitsk and Mainz in direct neutrino mass measurements via the endpoint of the tritium beta spectrum (see refs. [21,22], and further references therein). A planned upgrade of the neutrino mass spectrometer, KATRIN, will be based on the same principle [23]. An upcoming project at the CERN facility ISOLDE will employ the new retardation spectrometer WITCH, designed at Leuven University, to measure a in several allowed nuclear beta decays [24].

A proton detection trapping method, using a constant magnetic guiding field perpendicular to the neutron beam, was employed in the neutron lifetime measurement of ref. [20] (a rough measurement of the integral proton energy spectrum was also performed with the apparatus described in this article). Recently, a was measured in neutron decay using a prototype proton retardation spectrometer of a group from Sussex [16,25,26], employing the same trapping technique that was used in ref. [20]. This first determination of a did not lead to a significant improvement of the accuracy attained in the earlier experiment by Stratowa *et al.* [15]. The spectrometer *a*SPECT has been designed to remedy the shortcomings of its predecessor. We plan to measure a with an absolute experimental uncertainty of at least $\delta a \approx 3 \times 10^{-4}$, from which the coupling constant ratio λ_a can be determined with an accuracy of $\delta\lambda_a \approx 0.001$. For this purpose we need 10^9 decay events, which can be obtained within 25 days beamtime in the Institute Laue-Langevin (our expected decay rate is about 500 Hz).

3 The adiabatic transmission function

The adiabatic approximation for charged particle motion in electric and magnetic fields provides a suitable framework for a comprehensive spectrometer design. *a*SPECT therefore was designed such that the decay protons fulfill the adiabatic condition. Analyses of this concept can be found in many places (see, *e.g.* refs. [18,27–29]). The helical motion induced by the Lorentz force is called adiabatic if the relative spatial changes of the magnetic and electric fields stay small during one particle gyration: $\Delta B/B \ll 1$ and $\Delta E/E \ll 1$. The radius of the particle orbit thus changes only slowly.

It is useful to decompose the proton kinetic energy T into transverse and longitudinal components, $T_\perp = T\sin^2\theta$ and $T_\parallel = T\cos^2\theta$, with θ denoting the angle between the proton momentum vector and the magnetic field direction. The orbital magnetic moment $\mu = T_\perp/B$ is in the adiabatic approximation constant (this expression for μ is valid in the non-relativistic approximation, which we use for the calculations of proton motion). Using conservation of μ and energy, the adiabatic longitudinal energy $T_\parallel^\mathrm{ad}$ (meaning $T_\parallel$ calculated in the adiabatic approximation) at any trajectory point $\mathbf{P}$ can be expressed as

$$T_\parallel^\mathrm{ad}(T_0) = T_0 - e(U - U_0) - \frac{B}{B_0} T_0 \sin^2\theta_0. \qquad (3)$$

Here, T_0 is the proton kinetic energy at the decay point $\mathbf{P}_0$, and θ_0 is the angle between the proton velocity vector and the magnetic field line at $\mathbf{P}_0$. B_0 and U_0 denote the values of the magnetic-flux density and the electrostatic potential at $\mathbf{P}_0$, and B and U are the corresponding values at $\mathbf{P}$. The proton is transmitted if $T_\parallel^\mathrm{ad} > 0$ at any trajectory point between $\mathbf{P}_0$ and the detector. If $T_\parallel^\mathrm{ad}$ becomes zero somewhere, the proton is reflected at this point. It was an important design goal to avoid a situation where protons with sufficient energy to pass the potential barrier may be reflected outside the analyzing plane.

The analyzing plane is situated in the middle of the central electrode at $z \approx 130$ cm (see fig. 1). At the intersection point of a trajectory through the analyzing plane the electrostatic potential is denoted by U_A and the magnetic field by B_A. We define the adiabatic transmission energy T_tr as the solution of $T_\parallel^\mathrm{ad}(T_\mathrm{tr}) = 0$ with $U = U_\mathrm{A}$ and $B = B_\mathrm{A}$:

$$T_\mathrm{tr} = \frac{e(U_\mathrm{A} - U_0)}{1 - \frac{B_\mathrm{A}}{B_0}\sin^2\theta_0}. \qquad (4)$$

Thus, the transmission energy T_tr is a function of $\cos\theta_0$ as shown in fig. 2. $T_\mathrm{tr} = T_\mathrm{tr}^\mathrm{min}$ is reached at $\cos\theta_0 = \pm 1$, whereas at $\cos\theta_0 = 0$ we have $T_\mathrm{tr} = T_\mathrm{tr}^\mathrm{max}$, with the values given by

$$T_\mathrm{tr}^\mathrm{min} = e(U_\mathrm{A} - U_0), \quad T_\mathrm{tr}^\mathrm{max} = T_\mathrm{tr}^\mathrm{min}/(1 - B_\mathrm{A}/B_0). \qquad (5)$$

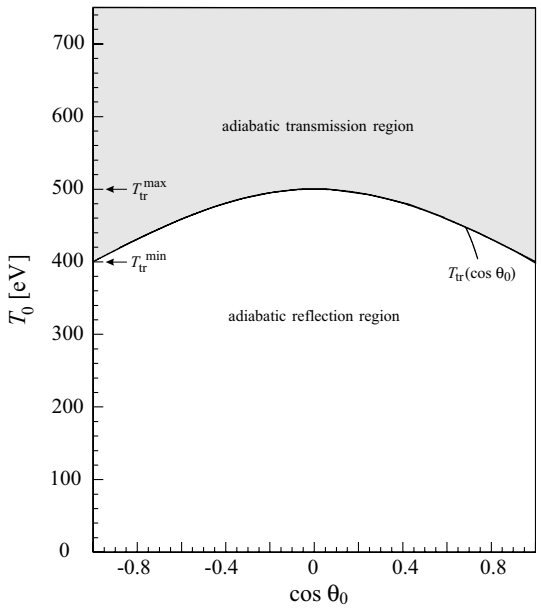

Fig. 2. The plane of the proton kinetic energy T_0 and the cosine of the proton starting angle θ_0 with respect to the magnetic field at the decay point. In the adiabatic approximation, protons with $T_0 > T_{\rm tr}(\cos\theta_0)$ (with $T_{\rm tr}$ defined in eq. (4)) will be transmitted by the potential barrier, whereas those with $T_0 < T_{\rm tr}$ will be reflected. The line $T_{\rm tr}(\cos\theta_0)$ is shown for $U_{\rm A} - U_0 = 400\,{\rm V}$.

*a*SPECT is designed such that all protons with $T_0 > T_{\rm tr}$ are transmitted. According to eq. (4), the values of the potential and the magnetic field have to be known accurately only in the decay volume and in the analyzing plane. At all other trajectory points, a rough knowledge of them is sufficient: we just have to make sure that an inequality, the adiabatic transmission condition $T_\parallel^{\rm ad}(T_{\rm tr}) \geq 0$, is fulfilled everywhere. If, for example, the target value of $T_\parallel^{\rm ad}(T_{\rm tr})$ is 10 eV at some point between the decay region and the analyzing plane, the potential U at this point should be known within a few volts. Note that, if the adiabatic transmission condition is fulfilled for $\theta_0 = 90°$, it is fulfilled also for all other starting angles.

Next, we consider the proton detection rate $\rho(U_{\rm A})$, as a function of the analyzing plane potential. The theoretical proton recoil spectrum $w_{\rm p}(T_0)$, including recoil-order, Coulomb and model-independent radiative corrections, can be found in ref. [30][1]. The spectrum is shown in fig. 3. Its endpoint $T_{\rm m}$ is given by

$$T_{\rm m} = \frac{(m_{\rm n} - m_{\rm p})^2 - m_{\rm e}^2}{2m_{\rm n}}, \tag{6}$$

where $m_{\rm n}$, $m_{\rm p}$ and $m_{\rm e}$ are the neutron, proton and electron mass, respectively (we use natural units with $c = 1$).

[1] The proton spectrum with recoil-order correction can be found in ref. [31]. Nachtmann published a proton spectrum formula including both recoil-order and Coulomb corrections in ref. [32]. A sign error in this formula was found by C. Habeck [33] (in the last line of eq. (4.5) in ref. [32] the expression $\sigma + x^2$ should be changed to $\sigma - x^2$).

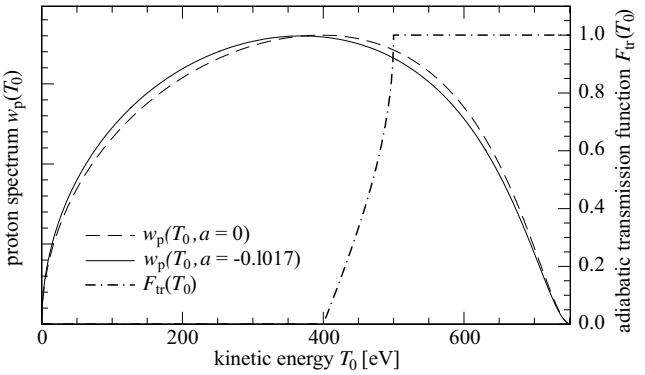

Fig. 3. The proton recoil spectrum, shown for two different values of a to demonstrate the sensitivity. The dashed-dotted line indicates the transmission function defined in eq. (10), for $U_{\rm A} - U_0 = 400\,{\rm V}$.

In order to compute the proton detection rate $\rho(U_{\rm A})$ in the adiabatic approximation, we have to integrate $w_{\rm p}(T_0)$ over the solid angle of the initial proton direction and over the initial kinetic energy T_0. The second integral extends from the θ_0-dependent $T_{\rm tr}$ up to $T_{\rm m}$:

$$\rho(U_{\rm A}) = 2\pi \int_{-1}^{1} {\rm d}\cos\theta_0 \int_{T_{\rm tr}}^{T_{\rm m}} {\rm d}T_0\, w_{\rm p}(T_0) \tag{7}$$

(the adiabatic transmission region defined by $T_0 > T_{\rm tr}$ can be seen in fig. 2). Since the proton recoil spectrum for unpolarized neutron decay has no angular dependence, the integration over $\cos\theta_0$ in eq. (7) can be done analytically. For this purpose, we introduce the transmission cosine function $c_{\rm tr}(T_0)$, defined for proton energies $T_{\rm tr}^{\rm min} \leq T_0 \leq T_{\rm tr}^{\rm max}$, by inverting $T_0 = T_{\rm tr}(\cos\theta_0)$:

$$c_{\rm tr}(T_0) = \sqrt{1 - \frac{B_0}{B_{\rm A}}\left(1 - \frac{T_{\rm tr}^{\rm min}}{T_0}\right)}. \tag{8}$$

For a starting energy T_0 within the above interval, protons with $|\cos\theta_0| > c_{\rm tr}(T_0)$ can pass the analyzing plane. In this case the angular integration in eq. (7) gives simply a factor $2(1 - c_{\rm tr}(T_0))$. For $T_0 > T_{\rm tr}^{\rm max}$ this factor is 2, and for $T_0 < T_{\rm tr}^{\rm min}$ it is zero. Therefore, we simply obtain

$$\rho(U_{\rm A}) = 4\pi \int_{0}^{T_{\rm m}} {\rm d}T_0\, w_{\rm p}(T_0)\, F_{\rm tr}(T_0), \tag{9}$$

where the adiabatic transmission function $F_{\rm tr}(T_0)$ is defined as

$$F_{\rm tr}(T_0) = \begin{cases} 0, & \text{if } T_0 \leq T_{\rm tr}^{\rm min}, \\ 1 - c_{\rm tr}(T_0), & \text{if } T_{\rm tr}^{\rm min} < T_0 < T_{\rm tr}^{\rm max}, \\ 1, & \text{if } T_0 \geq T_{\rm tr}^{\rm max}. \end{cases} \tag{10}$$

This function is shown in fig. 3 for $U_{\rm A} - U_0 = 400\,{\rm V}$ (with $B_0/B_{\rm A} = 5$), together with the proton spectrum.

Deviations from adiabatic motion, proton scattering on residual gas molecules and other effects may influence

the transmission function and therefore falsify the interpretation of the measured proton rates. These points will be further discussed in sect. 5.

At this point, we can include in our discussion non-uniformities of the electrostatic potentials and magnetic field values in the decay volume and at the analyzing plane. In general, the adiabatic transmission function depends on the fields U_0, B_0, U_A and B_A, corresponding to various points $\mathbf{P}_0$ within the decay volume. It has to be averaged over the decay volume, which includes weighing with the neutron density $n(\mathbf{P}_0)$. If the fields were perfectly uniform there, the neutron density function would simply drop out. However, as discussed in the next section, the designed homogeneity of the magnetic field in the decay volume and in the analyzing plane is worse than the uniformity of the electrostatic potential. Therefore, it will be necessary to know the spatial dependence of the neutron density to some extent. Keeping the field variations sufficiently small, however, we avoid the need to make very accurate density measurements.

The correlation coefficient a can be determined from measurements of the decay rate $\rho(U_\mathrm{A})$ for various settings of U_A. In ref. [17], a specific count rate ratio was considered and its sensitivity to a was demonstrated. An uncertainty of the potential difference $U_\mathrm{A} - U_0$ of 10 mV and an uncertainty of the magnetic field ratio B_A/B_0 of 10^{-4} would each correspond to an uncertainty in a of 10^{-4}.

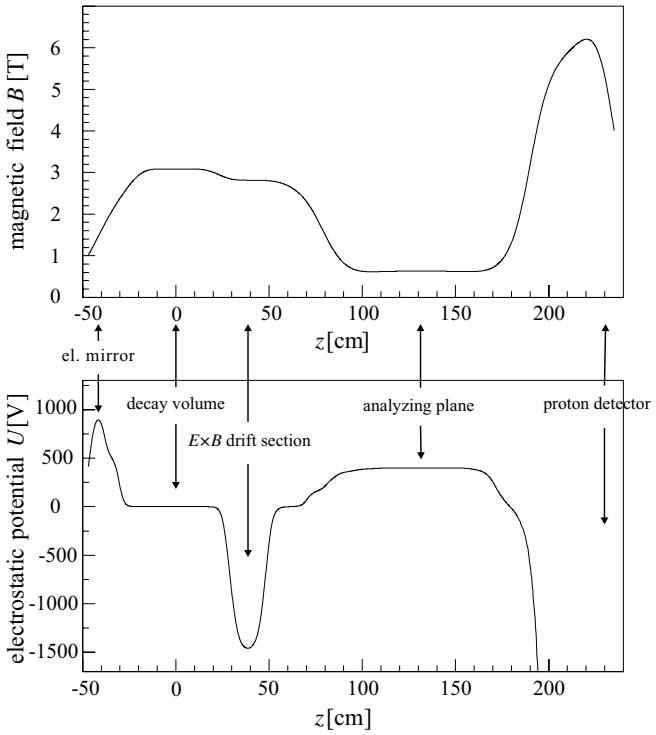

Fig. 4. The values of the magnetic field and the electrostatic potential on the z-axis of the spectrometer. The corresponding potentials of the electrodes are shown in fig. 1.

4 Spectrometer design

4.1 The neutron decay volume

The decay volume (see fig. 1) is a cylinder with a length of 8 cm along the z-axis and a diameter of 3 cm. The radial extent is defined by a thin circular diaphragm, to be placed at the end of the electrode e6 ($z = 25$ cm). The magnetic field lines connecting the decay volume and the detector through this diaphragm define what we call a flux tube. The long dashed lines in fig. 1 are calculated field lines, they indicate the approximate size of the flux tube. The sensitive area of the detector has to be sufficiently large to detect all protons which pass through diaphragm and potential barrier.

4.2 The electrode system

The design of the electrode system can be seen in fig. 1. The electrostatic potential on the z-axis of the spectrometer is shown in the lower part of fig. 4. The electrodes have cylindrical shape (but not all of them are axially symmetric). The mirror electrodes e1 and e2 will be held at 1 kV and 500 V, respectively, in order to reflect all decay protons starting towards them. The electrodes e3-e6 are at ground potential. They shield the decay volume from electric fields of the other electrodes. According to our calculations, the electrostatic potential within the decay volume is smaller than 1 mV, which is well within the tolerance. Our electric-field calculation method is described in appendix A.1.

The long central electrode e14 defines the value of the analyzing potential U_A. Set for instance to 400 V, the potential in the center of the analyzing plane is only by 2 mV smaller than at the surface of the electrode, the difference being due to field penetration from the neighbouring electrodes. The electrostatic potential within the analyzing plane is thus sufficiently uniform. For different values of U_A, the potentials of the electrodes e10-e15 have to be changed in such a way that their ratios are kept constant. Then the adiabatic transmission condition is always fulfilled.

The electrodes e8 and e16 are dipole electrodes, each consisting of two half-cylinders, which may be held at different potentials. This produces an electric field perpendicular to the magnetic field, giving rise to an $\mathbf{E} \times \mathbf{B}$ drift. The electrode e8 thus removes the protons which otherwise would remain trapped between the electrostatic mirror and the potential barrier. Note that the $\mathbf{E} \times \mathbf{B}$ drift does not depend on the direction of proton motion through the dipole electrode, and several passages through the electrode will remove all of them. The trapping time of these protons decreases with increasing dipole potential $|U_8|$. A potential difference up to 3 kV may be applied to e8 in order to keep non-adiabaticity within the acceptable limit. This large dipole potential at e8 is advantageous in order to reduce the systematic effect due to the proton collisions with the residual gas molecules (see sect. 5.3 for details).

The calculations showed that the grounded electrodes e7 and e9 strongly improve the adiabaticity of the protons, which acquire large longitudinal momenta in e8 due to the

negative potential. The electrode e16 causes a transverse drift of the protons which have passed the potential barrier. With a potential difference of about 20 kV they are deflected by several mm, whereas the much faster electrons stay essentially undeflected. Hence, a proton and an electron emitted from the same neutron decay will hit the detector at different positions of the detector. The advantage of this behaviour will be explained below.

Finally, in order to detect the protons, they are accelerated to an energy of about 30 keV by the negative potential of the electrode e17.

4.3 The superconducting coil system

The design of the superconducting coil system can be seen in fig. 1. The coil system and its magnetic field are axially symmetric. All the coils except c5 and c6 will be connected in series. As an important advantage, the ratio $B_{\rm A}/B_0$, which enters the transmission function defined in eq. (10) is independent of the exact value of the current. Slow drifts during data taking thus will not do any harm. For the design of the coils, we assumed a maximum allowed current of 100 A in a wire with a cross-section of 0.39 mm^2. This (still conservative) limit is set by the critical current density of the superconducting wire. The magnetic field on the z-axis of the spectrometer can be seen in the upper part of fig. 4 (for details about the magnetic-field calculation method see appendix A.2).

The coils provide a homogeneous magnetic field in the decay volume and in the analyzing plane. The magnetic field on the symmetry axis in the decay volume is shown in the upper part of fig. 5. Here the coils c1-c4 and c7-c9 provide a field which has a maximum at $z = 0$ cm, and no local minima within the entire decay volume. One can see in fig. 5 that the level of homogeneity (the relative change) of the magnetic field inside the decay volume is better than 10^{-4}. A rather homogeneous field is also provided in the region of the dipole electrode e8. In this way a large potential difference can be used there without any significant influence on the adiabaticity. Our coil design computation method, which provides the necessary homogeneity values, is explained in appendix A.4.

The small compensation coils c5 and c6 are powered independently and separately. They can provide a field up to 1% of the main field, and act as trim coils to adjust the field within the decay volume. As shown in the upper part of fig. 5, it is thus possible to provide a slight axial field gradient there, with the field decreasing towards the detector. Thus trapping of decay protons by the magnetic mirror effect between the decay volume and the electrostatic mirror (electrode e1), which would strongly affect the transmission function, is avoided. Changing the current settings of the coils c5 and c6 allows us to change B_0 up to 1% (by using 100 A current). This provides a useful means to quickly perform a statistically significant test of the computed transmission function. A similar change of $B_{\rm A}$ would also be possible at the analyzing plane, using additional external coils there (not shown in fig. 1).

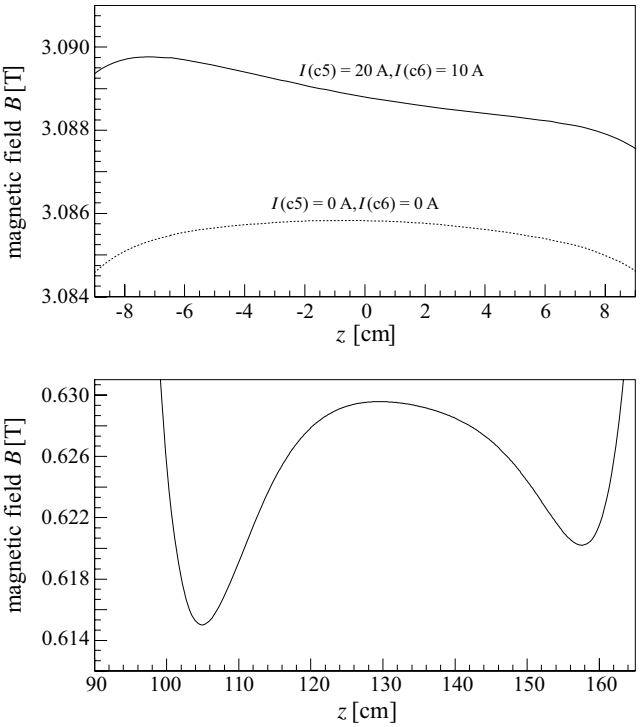

Fig. 5. The magnetic field on the z-axis in the decay volume, shown for two different current settings of the auxiliary coils c5 and c6 (upper figure), and at the analyzing plane (lower figure).

The expected magnetic-flux density in the region around the analyzing plane is plotted in the lower part of fig. 5. There, the level of inhomogeneity of the magnetic field (the relative difference of $B_{\rm A}$ on the axis and on the outermost off-axis points in the analyzing plane) is about 2×10^{-4}. Close to the analyzing plane, the electrostatic potential is nearly uniform, $U \approx U_{\rm A}$. If the magnetic field had a minimum there, it would have to be extremely shallow in order to fulfill the transmission condition. Therefore, we have designed the magnetic field to have a local maximum there. Then the adiabatic transmission condition close to the analyzing plane is automatically fulfilled, as can be seen from the following argument: the condition $T_{\parallel}^{\rm ad}(T_{\rm tr}) > 0$ (see eqs. (3) and (4)) requires

$$\frac{B_0 - B\sin^2\theta_0}{B_0 - B_{\rm A}\sin^2\theta_0} > \frac{U - U_0}{U_{\rm A} - U_0}\,. \tag{11}$$

The right-hand side of this equation around the analyzing plane is less than unity, since $U_{\rm A}$ is the maximum of the potential. Hence, the inequality is automatically fulfilled if the left-hand side is larger than 1, that is if $B < B_{\rm A}$.

In the detector region the magnetic field is about twice as large as in the decay volume (see fig. 4). For the decay protons, the accelerating voltage of electrodes e16 and e17 overcomes the effect of the magnetic mirror. The smaller diameter of the flux tube in the high magnetic field enables us to use a smaller detector. Secondly, the electron background gets significantly reduced by the magnetic mirror (see also sect. 5.4).

4.4 The proton detector

To detect the decay protons, a segmented silicon PIN diode with a total area of $26 \times 26\,\mathrm{mm}^2$ is used. It is divided into 25 strips of $0.8 \times 25\,\mathrm{mm}^2$ each, providing spatial resolution in one dimension. The segmentation serves two main purposes: it reduces the capacitive noise of the detector, and it can help to suppress the background caused by electrons from neutron decay. The background suppression is achieved by the $\mathbf{E}\times\mathbf{B}$ drift as described in sect. 4.2. When hitting the detector, the electron and the proton created in one decay event will be spatially separated far enough to create signals in two different strips of the detector. The protons have to penetrate through a protective layer of Si_3N_4 with a thickness of 40 nm, followed by a layer consisting of SiO_2 with a thickness of 27 nm. The total dead layer of 67 nm induces an approximate energy loss of 10 keV for protons with energy 30 keV. They are detected by an $0.5\,\mu$m P^+ implanted layer, the $380\,\mu$m thick substrate and an $0.5\,\mu$m thick N^- layer, coated by an $0.7\,\mu$m Al layer for contacting the detector from the backside.

From the characteristics of our electronics, we expect the detector resolution to be about 4 keV (FWHM). In test experiments with this kind of detector (but using standard, non-optimized electronics), we have seen the proton peak well above 1σ of the noise.

5 Systematic effects

5.1 Adiabatic transmission function

In order to keep systematic uncertainties of the correlation coefficient a well below $\delta a \approx 3\times10^{-4}$, we have to know the size of the magnetic field B_0 in the decay volume and B_A in the analyzing plane with a relative accuracy of 10^{-4}. Since magnetic-field measurement during the data taking is not feasible, we need a good stability (small time dependence) of the magnetic field. In addition, the inhomogeneity of the magnetic field in these regions should not be much larger than 10^{-4}, otherwise an accurate measurement for the neutron density distribution inside the decay volume is necessary.

The potential U_0 in the decay volume is smaller than 1 mV, and the variations of the potential U_A at the analyzing plane are smaller than 2 mV. Therefore, the electric potentials U_0 and U_A are well defined by the electrode voltage values, and their homogeneity within the above regions is sufficient. The voltage of the central electrode e14 has to be known to an absolute accuracy of 10 mV. In principle, the accumulation of negative space charges around the analyzing plane could change the electric potential U_A. Experiences in comparable experiments [16,22] let us expect that the accumulation rate is sufficiently small that they can be removed by an occasional reversing of all electrode potentials. Since all electrodes are gold-coated and kept at the same temperature, the work function differences of the different materials cancel. Surface charging on the insulating surface layer of the electrodes would influence the electric potential in the vacuum. Measurements of this effect due to external radiation for different surfaces are presented in ref. [34]. Based on extrapolation of these results to our case we expect this effect to be negligible. In addition, we are planning to construct a monochromatic electron source to measure the potential difference between the decay volume and the analyzing plane *in situ*.

5.2 Non-adiabatic proton motion

The electromagnetic field of *a*SPECT is designed in such a way that non-adiabatic effects are negligible. Breakdown of the adiabatic approximation would cause the transmission function to be different from the adiabatic transmission function calculated in eq. (10). This effect can be calculated for given field maps of the electric potential and the magnetic field within the flux tube. Using this information, an optimisation procedure to suppress non-adiabaticity effects down to the required level was established.

In sect. 3 we have stated that the orbital magnetic moment $\mu = T_\perp/B$ is constant in the adiabatic approximation. The calculations show that in the analyzing plane the value of μ is indeed close to its value at the decay point (our trajectory calculation method is explained in appendix A.3). On the other hand, in the regions with high electric-field and magnetic-field gradient, the value of μ oscillates with a period equal to the local gyration period, and the oscillation amplitude increases with the field gradients. As explained in refs. [27–29], the adiabatic invariant $\hat{\mu} = \mu + \delta\mu$ varies much less than μ. The term $\delta\mu$ is a complicated expression, proportional to the first and higher derivatives of the magnetic field and the electrostatic potential. Inside homogeneous field regions these derivatives are small, and therefore $\mu \approx \hat{\mu}$. When a proton moves from one homogeneous field region to another, its orbital magnetic moment can regain the starting value with high accuracy, although between these two regions, where the field gradients are large, μ can have large oscillations ($\delta\mu$ has larger changes here, and since the adiabatic invariant is almost constant, the orbital magnetic moment should also change). The charged particles seem to have "memory" [27]: in passing from one homogeneous field region to another they remember their original orbital magnetic moment.

The non-adiabaticity effect is more severe for the trapped protons than for the transmitted ones. The trapped protons perform some axial oscillations between the electrostatic mirror and the analyzing plane before being removed due to the dipole field of the electrode e8. The non-adiabatic change of the angle and of the orbital magnetic moment of the protons increases with the number of these oscillations (see ref. [16]). From this point of view it is advantageous to use a high dipole potential $|U_8|$, since the average number of axial oscillations decreases with increasing $|U_8|$. However, our trajectory calculations show that breakdown of the adiabatic approximation sets a limit of -3 kV for U_8. Acceleration of the protons increases their gyration length, and as a

Table 1. Systematic effect δa due to non-adiabatic motion for different B_0 magnetic field values, with $U_8 = -3\,\mathrm{kV}$ dipole potential (the $B_0/B_A = 5$ ratio is fixed).

B_0	3 T	1.5 T	1.2 T	0.9 T	0.6 T
δa	10^{-6}	$4 \cdot 10^{-5}$	$5 \cdot 10^{-4}$	$4 \cdot 10^{-3}$	$2 \cdot 10^{-2}$

consequence the deviation from the adiabatic approximation also increases. With this $-3\,\mathrm{kV}$ dipole potential the trapped protons make less than five to six axial oscillations between the electrostatic mirror and the analyzing plane before leaving the flux tube.

The non-adiabaticity effect on the orbital magnetic moment is expected to increase exponentially with decreasing magnetic field [29]. With the setting $U_8 = -3\,\mathrm{kV}$ we have computed the change of the extracted a value due to the deviation from adiabatic motion for several different magnetic field values B_0. All magnetic field values in the spectrometer were scaled by a common factor (this can be realized by changing the current in the coils). The results can be found in table 1. One can see that the systematic effect due to non-adiabaticity is negligible above $B_0 = 1.5\,\mathrm{T}$, but below $B_0 = 1\,\mathrm{T}$ it becomes substantial.

5.3 Residual gas

The protons may interact with the residual gas molecules. Three different kinds of collision can be distinguished: the protons may be neutralised by charge exchange processes, or change their energy and direction due to elastic or inelastic scattering. Protons with starting energy $T_0 > T_{\mathrm{tr}}$ should reach the detector without collisions, but charge exchange and energy loss processes may prevent them from doing so. In addition, changes of the pitch angle θ and energy T due to elastic scattering of protons affect the proton motion (θ is the angle between the proton momentum and the magnetic field). The elastic scattering has an effect on the transmission properties of all protons with $T_0 > T_{\mathrm{tr}}^{\mathrm{min}}$. All these effects on the transmission function were investigated.

The systematic effect due to these collisions is proportional to the residual gas density, and for a fixed temperature therefore to the pressure. We define p_{cr} as the critical value of the residual gas pressure at which a considered type of collision introduces a systematic effect on the parameter a at a level $\delta a = 10^{-4}$. Our values for p_{cr} are given at 60 K, which will be the temperature in the central bore of the cryostat. We report below the results of Monte Carlo calculations for the various processes, where we generated protons with various starting energies and angles in the decay volume and followed their trajectories. The calculations were performed by using published integral and differential cross-sections.

a) *Elastic scattering*
Elastic scattering processes change energy T and pitch angle θ of the protons. Due to elastic scattering, the protons with $T_0 > T_{\mathrm{tr}}$ could be hindered to pass the analyzing plane, and the trapped protons with $T_{\mathrm{tr}}^{\mathrm{min}} < T_0 < T_{\mathrm{tr}}$ could be transmitted. The effect on the trapped protons is more important, since in the absence of scattering they perform several axial oscillations between the electric mirror and the central electrode, and so the time they spend under the influence of the residual gas is much longer. The scattering probability of a trapped proton is proportional to its path length and therefore to the time it spends within the flux tube. The $\mathbf{E} \times \mathbf{B}$ drift perpendicular to the z-axis generated by the dipole electrode e8 removes the trapped protons from the flux tube after a few axial oscillations. The trapping time decreases with increasing dipole potential $|U_8|$ of this electrode. In an axially symmetric field configuration without $\mathbf{E} \times \mathbf{B}$ drift this time would be very large, so a large systematic effect due to elastic scattering might occur.
In order to calculate p_{cr} for elastic scattering, we need to know the differential elastic cross-section, for which we have used the tabulated values for elastic p-H_2 collisions given in ref. [35] (see also ref. [36]). The theoretical differential and integral cross-sections reported in these references are in good agreement with measurements and with other calculations. The critical pressure values for three different dipole potentials can be found in table 2 (the upper limit, $U_8 = -3\,\mathrm{kV}$, is given by the adiabaticity requirement).
Obviously, using a larger dipole potential will allow us to tolerate a larger residual gas pressure. With the help of the dipole electrode e8 we are able to obtain experimental information about this effect: we make measurements with large and with small dipole potential values, and compare the two fitted a values.

Table 2. Critical pressure values of elastic p-H_2 scattering for different dipole potentials U_8 (the typical differential cross-section here is around $10^{-13}\,\mathrm{cm}^2$/steradian).

U_8 (kV)	p_{cr} (mbar)
-3	$5 \cdot 10^{-8}$
-0.3	10^{-8}
-0.03	$1.4 \cdot 10^{-9}$

b) *Inelastic energy loss*
We have made calculations for inelastic scattering of protons on hydrogen molecules. We neglected here the change of the pitch angle θ, since the main systematic effect of the inelastic as well as the elastic scattering comes from changes of θ below a few degrees. The differential cross-section of elastic scattering in this angular region is considerably larger than that for vibrational excitation [37], and that was already discussed in the previous section.
The cross-sections for rotational and vibrational excitations are large [38,39], while we can safely neglect electronic excitation and ionisation for protons below 1 keV kinetic energy. The proton energy loss due to rotational and vibrational excitations is in the range 50–1000 meV. Excitation of vibrations in p-H_2 scattering

Table 3. Critical pressure values of the charge exchange process for different gases (the typical cross-section is around $10^{-16}\,\mathrm{cm}^2$).

Gas	p_{cr} (mbar)
H_2	$2 \cdot 10^{-8}$
Ar	10^{-8}
N_2	$2 \cdot 10^{-8}$
O_2	$4 \cdot 10^{-8}$
He	10^{-6}

is the more severe effect on proton energy loss, and it sets a limit of $p_{\mathrm{cr}} = 4 \times 10^{-8}$ mbar.
In addition to H_2, the residual gas can of course contain other components, and it would be important to extend these calculations later to other atoms and molecules.

c) *Charge exchange*
The moving proton may capture an electron from a gas molecule, resulting in a neutral hydrogen atom and a positive molecular ion with very low energy: $\mathrm{p} + \mathrm{M} \rightarrow \mathrm{H} + \mathrm{M}^+$. If the process occurs between the decay volume and the analyzing plane, no event will be detected. The cross-section of this reaction as a function of the proton kinetic energy may be found in refs. [38–40]. In our simulations, we obtained the values for the critical pressure of a few gases quoted in table 3. One can see that for He the charge exchange effect is much smaller than for the other gases (this is mainly due to the high ionization energy of the He atom).

5.4 Background

Discussing the background problem, we have to distinguish between correlated and uncorrelated background events. In neutron decay, electrons and protons are created simultaneously, and a fraction of the electrons will reach the detector, causing background signals correlated with a proton event. Uncorrelated events are due to positive ions coming from residual gas and electrodes, γ radiation and high-energy electrons created by neutron capture and by cosmic rays. Beam-related background, which is often a problem in neutron decay experiments, is not treated differently from environmental background in our analysis: in a straightforward strategy one measures the background separately from the signal and subtracts it. A potential of 1 kV between the decay region and the analyzing plane, *e.g.* at the electrode e10, will completely block the decay protons from reaching the detector. Of course, we have to make sure that this does not change the background which we want to measure. Additional studies are therefore required, like, *e.g.*, applying the blocking potential at different positions.

Background positive ions coming from the decay region have mostly very low energies. This background may be efficiently reduced if measurements of the rates $\rho(U_{\mathrm{A}})$ are taken for U_{A} not less than $\approx 40\,\mathrm{V}$. The validity of this conclusion has to be checked experimentally.

Correlated electron events could cause problems, since they occur in near coincidence with proton events. The minimum time of flight of the protons from the decay volume to the detector is about $5\,\mu$s, whereas the electrons move much faster. If protons were detected by a single detector with too large dead time, some of the protons would stay undetected. This would induce a serious systematic effect. Using a segmented PIN diode detector in combination with the $\mathbf{E} \times \mathbf{B}$ drift regions already discussed avoids this possible problem. The particles will be detected in different segments, and the detector deadtime does not matter. In such a scheme, the correlated events are easily identified among the other events due to their particular signature. This will be very useful as an aid to fully understand the background.

5.5 Doppler effect due to neutron motion

The Doppler broadening of the optical lines due to the thermal motion of atoms or molecules is a well-known phenomenon in spectroscopy. In beta decay processes, the motion of the decaying particle also changes the observed energies of the outgoing particles relative to the energies in the center-of-mass system (CMS) of the decaying particle. This change may affect the transmission function, and therefore it is considered here.

Neutrons from a cold-neutron beam have an average kinetic energy of about $T_{\mathrm{n}} = 5\,\mathrm{meV}$. A proton having a CMS energy of $T_{\mathrm{CMS}} = 400\,\mathrm{eV}$ and being emitted in the direction of flight of the decaying neutron has in the laboratory system an energy $T_{\mathrm{LAB}} = T_{\mathrm{CMS}} + \delta T$, with $\delta T = 2\sqrt{T_{\mathrm{n}} T_{\mathrm{CMS}}} \approx 2.8\,\mathrm{eV}$. Compared to the required 10 meV accuracy of the proton CMS energy determination, this energy change is enormous. If we would use a neutron beam parallel to the magnetic field and without an electrostatic mirror, the systematic correction for this effect would thus require a very accurate measurement of the neutron velocity spectrum.

In *a*SPECT the beam is transverse to the neutron beam, and protons are detected with 4π acceptance. Since protons emitted in a direction opposite to the neutron motion have smaller laboratory energy than their CMS energy, we have a large cancellation of Doppler effects. Using a typical neutron velocity distribution, we have calculated its effect on a for different settings of the analyzing potential U_{A}. Below $U_{\mathrm{A}} = 500\,\mathrm{V}$ it is smaller than 10^{-4}, so we do not expect any essential systematic uncertainty from this effect.

5.6 Edge effect

The diaphragm placed at the end of electrode e6 (defining the decay volume) may induce another systematic effect. Since the radius of gyration of a proton depends on its energy, proton absorption by the edge of a thick diaphragm leads to an energy-dependent size of the flux tube and

hence the decay volume. However, protons with energies below 1 keV are absorbed in a very thin layer of material well below one micron. A diaphragm with a few microns thickness, compared to a gyration length of several millimeters, induces an edge effect far below the required limit if the neutron beam density is homogeneous. The edge effect is sensitive to the inhomogeneity of the neutron density inside the decay volume, and this density should be determined to a few percent accuracy, in order that the edge effect contribution for the parameter a should be not larger than 10^{-4}. The latter kind of edge effect is inversely proportional to B_0^2, therefore a smaller magnetic field would require a more accurate neutron density measurement.

5.7 Detector efficiency

While the average efficiency of the proton detector drops out of the ratios of measured count rates, we have to consider a possible dependence on proton energy or impact angle. Both effects have an influence on the measured proton rate ratio and have to be taken into account.

Since the impact energy will be close to the acceleration voltage of 30 kV, and the range of kinetic energies of the decay protons is only 750 eV, we may write the energy-dependent detection efficiency in the form $f_{\text{impact energy}} \propto (1+c_1 \cdot T_0)$, with c_1 being a small number. At a level of tolerance $\delta a = 10^{-4}$, we obtain the condition $|c_1| < 200\,\text{ppm/keV}$. An energy-dependence of the detector efficiency is expected due to backscattering. We will discuss it below. A second effect is due to the electronic threshold to separate proton signals from the noise. As discussed in sect. 4.4, our silicon detector will have an energy resolution good enough to result in a sufficiently low number of proton signals below the trigger level.

The main contribution to the angular dependence is due to backscattering in the dead layer. We thus expect a dependence of the form $f_{\text{impact angle}} \propto (1 - c_2/\cos\gamma)$, where γ is the angle of the proton relative to the detector axis and c_2 is a constant which should be small. Due to the acceleration of the protons in the electrostatic field of the detector electrode, the maximum value for γ is of the order of 10 degrees. At our level of tolerance, we have to specify $c_2 < 7 \cdot 10^{-3}$.

In our simulations we took protons which are impinging to the surface of the detector. They had to penetrate the different detector layers as described in sect. 4.4. For the purpose of our analysis we evaluated the energy loss and the backscattering probability[2] in steps of 0.1 nm. For each backscattered proton we determined if there is enough energy deposited in the active part of the detector to be detected. Since only one out of 1000 protons is backscattered, we could neglect multiple backscattering events.

[2] The energy loss in the different layers was calculated with the help of the program SRIM2003. The backscattering probablity was calculated using a modified Rutherford formula which takes into account the screening of the Coulomb potential of the nucleus due to the electrons [41].

The result of these simulations is that $c_1 \sim 200\,\text{ppm/keV}$ and $c_2 = 8 \cdot 10^{-4}$. These values fulfill our requirements. In addition, both quantities will be measured in a separate experiment.

6 Conclusions

The accurate measurement of the neutrino-electron correlation parameter in neutron decay is important in order to determine precisely the element V_{ud} of the CKM quark-mixing matrix, and thus to test the unitarity of this matrix, which is a fundamental part of the Standard Model of particle physics. We believe that the retardation spectrometer aSPECT described in this paper is suitable for this purpose. The superconducting coil and electrode system of aSPECT were designed in a way to minimize the various systematic effects. Construction of this spectrometer is under way.

This work was supported by the German Federal Ministry for Research and Education under Contract No. 06MZ989I and 06MT196, and by the University of Mainz.

Appendix A. Field, trajectory and design calculations

Appendix A.1. Electric fields

A new computation method for the electric field of axially symmetric electrode systems has been developed [42]. It is based on the charge density (or boundary element or integral equation) method. The calculation contains three main steps. First, the charge density is computed on the electrode surfaces. For this purpose, the electrode surfaces are meshed, and a linear algebraic equation system has to be solved in order to obtain the unknown charge density values at the mesh points. The coefficients of the algebraic equation system are computed by Coulomb integration. Second, knowing the charge densities on the electrode surfaces, the electric potential Φ and its higher axial derivatives $\Phi_n := \partial_z^{(n)}\Phi$ $(n = 1, 2, \ldots)$ are calculated analytically with high accuracy in many axis points. Third, the electric potential and field at an arbitrary off-axis point inside the electrode system can be calculated by a Legendre-polynomial expansion, employing the numbers Φ_n corresponding to the closest axis point.

The computer program was tested by comparing its results with that of several published capacity and field calculations. The Legendre polynomial expansion at off-axis points was tested by a comparison with complementary field calculations using complete elliptic integrals (details will be published in ref. [42]).

In order to study the $\mathbf{E} \times \mathbf{B}$ drift effects, in the dipole-field electrode region we employed the following computation method: first we approximated the dipole electrode by a few hundred charged rectangles. The charge values for these sub-elements were then calculated using the charge density method, and their potentials and electric fields were evaluated analytically.

Using this method, a very smooth and precise electric-field calculation is possible, and this makes it possible to follow the trapped proton trajectories for a long time, without any substantial numerical errors (see below in appendix A.3).

Appendix A.2. Axially symmetric magnetic fields

The magnetic-field calculation of superconducting coils (without magnetic material) is simpler than the electric-field calculation, because in this case the source of the field (the current) is known; thus there is no need to solve an integral equation. The starting point of the calculation here is the thin axially symmetric solenoid. The magnetic field and its higher derivatives created by this solenoid on an arbitrary axis point can be expressed analytically (without numerical integration) by using the first derivatives of the Legendre polynomials. In the case of the thick coil a radial numerical integration is necessary. Then, for a system with several thick coils having a common symmetry axis, the magnetic field B and its higher axial derivatives $B_n := \partial_z^{(n)} B$ $(n = 1, 2, \ldots)$ are computed in many axis points.

Similarly to the electric field, the magnetic field at an arbitrary off-axis point inside the coil system can be computed by an expansion in terms of Legendre polynomials, using the B_n values at the closest axis point (see refs. [43, 44] for more details). This expansion was tested by comparing it with field calculations using complete elliptic integrals.

Appendix A.3. Trajectories

The trajectories of charged particles in the electric and magnetic field of the spectrometer were computed using an 8th order Runge-Kutta algorithm [45,46]. In order to improve its accuracy, we employed in our program also the analytical trajectory formula for constant electric and magnetic fields: the Runge-Kutta algorithm calculates only the rest of the motion (taking into account the change of the fields during a time step, which is about 20–30 times smaller than the gyration period defined by the magnetic field).

The energy and the canonical azimuthal angular momentum are exact constants in axially symmetric fields [47]: their change during the motion indicates the level of the numerical inaccuracy. Using the methods described above, it is possible to perform very accurate trajectory calculations: the relative change of these constants for trapped particle motions after several million gyrations was found to be at the 10^{-10} level. This high accuracy cannot be obtained by using the commercially available field and trajectory computation programs.

In *a*SPECT, the protons perform only a few axial oscillations inside the fluxtube, if a high dipole potential of the electrode e8 is employed. On the other hand, the effect of the elastic proton scattering with the residual gas molecules can be tested by using smaller dipole potential at e8. In this case, the protons are trapped inside the fluxtube for a longer time, and the change of their orbital magnetic moment by non-adiabatic effects has to be computed by a precise long-time trajectory simulation. The high accuracy of our field and trajectory calculation is also useful for background studies, where the trapping conditions of ions and electrons have to be investigated.

Appendix A.4. General procedure of the coil design

1. Symmetric double Helmholtz coils: c1-c4

A fourth-order homogeneous magnetic field (with vanishing second derivative at $z = 0$: $\partial_z^{(2)} B(0) = 0$) can be obtained by a single-Helmholtz-coil pair of finite cross-section [48]. Using a double-Helmholtz-coil pair system, an 8th-order symmetric field (with $\partial_z^{(n)} B(0) = 0$ for $n = 2, 4, 6$) can be created, which has a much better homogeneity [49]. As a first step, we have employed a constrained optimization program, which has found the geometrical dimensions of the symmetric c1-c4 coil system. The program minimized the total volume of the coils, with the following constraints: the magnetic field at $z = 0$ is $B(0) = 3\,\mathrm{T}$, $\partial_z^{(4)} B(0) = \partial_z^{(6)} B(0) = 0$, and the second derivative $\partial_z^{(2)} B(0)$ was constrained to have a small negative value, in order to obtain a field in the decay volume without local minima. Some practical constraints are also included into the program (for example: the superconducting coils should be inside the cryostat).

2. The coils c7 and c9

In the next step, we have chosen manually the dimensions of the coils c7 and c9. The coil c7 is necessary in order to obtain a nearly homogeneous field region around the dipole electrode e8. The coil c9 was chosen to get a large field at the detector.

3. The asymmetric c1-c4 coil system

The coils c7 and c9 make the system asymmetrical, therefore the homogeneous field at the $z = 0$ point can be created only by an asymmetrical c1-c4 coil system. The second optimization program searched the dimensions of this asymmetrical system, with similar constraints as described above. The asymmetrical optimization problem is more difficult than the symmetric one, since it has more free parameters, therefore it is advantageous to use the results of the symmetrical system as starting values for this computation.

4. The coil c8

We need a homogeneous field not only at $z = 0$, but also in the analyzing plane at about $z = 130\,\mathrm{cm}$. The coil c8 has the task to improve the homogeneity at this plane. For this purpose, the dimensions of the coils c1-c4, c7 and c9 were fixed, and the third optimization program searched the optimal dimensions of the coil c8.

5. Iteration of the second and third optimization programs

The coil c8 changes slightly the homogeneity at $z = 0$, so the second optimization program was run again. After 3

iterations of the second and third optimization programs a perfect convergence was obtained: the magnetic field had the required homogeneity in both the decay volume and at the analyzing plane.

A more detailed description of our coil design computation method will be presented in ref. [50].

References

1. J. Byrne, Rep. Prog. Phys. **45**, 115 (1982); *Neutrons, Nuclei and Matter* (IOPP, Bristol, 1995).
2. D. Dubbers, Prog. Part. Nucl. Phys. **26**, 173 (1991).
3. K. Schreckenbach, W. Mampe, J. Phys. G **18**, 1 (1992).
4. D. Dubbers, W. Mampe, J. Döhner, Europhys. Lett. **11**, 195 (1990); D. Dubbers, Nucl. Phys. A **527**, 239c (1991).
5. F.E. Close, Nucl. Phys. A **508**, 413 (1990).
6. J.D. Jackson, S.B. Treiman, H.W. Wyld, Phys. Rev. **106**, 517 (1957).
7. F. Glück, I. Joó, J. Last, Nucl. Phys. A **593**, 125 (1995).
8. B.G. Yerozolimsky, Nucl. Instrum. Methods A **440**, 491 (2000); B.G. Yerozolimsky, Yu.A. Mostovoi, Yad. Fiz. **53**, 418 (1991) (Sov. J. Nucl. Phys. **53**, 260 (1991)); Yu.A. Mostovoi, Phys. At. Nuclei **59**, 968 (1996).
9. B.G. Yerozolimsky *et al.*, Phys. Lett. B **263**, 33 (1991); **412**, 240 (1997).
10. K. Schreckenbach, P. Liaud, R. Kossakowski, H. Nastoll, A. Bussière, J.P. Guillaud, Phys. Lett. B **349**, 427 (1995); P. Liaud *et al.*, Nucl. Phys. A **612**, 53 (1997).
11. H. Abele, M. Astruc Hoffmann, S. Baeßler, D. Dubbers, F. Glück, U. Müller, V. Nesvizhevsky, J. Reich, O. Zimmer, Phys. Rev. Lett. **88**, 211801 (2002); H. Abele *et al.*, Phys. Lett. B **407**, 212 (1997).
12. I.S. Towner, J.C. Hardy, in *WEIN98 Conference Proceedings, Santa Fe, (1998)* (World Scientific, Singapore, 1999), arXiv:nucl-th/9809087; I.S. Towner, J.C. Hardy, J. Phys. G **29**, 197 (2003).
13. D.H. Wilkinson, Nucl. Instrum. Methods A **488**, 654 (2000).
14. Particle Data Group, K. Hagiwara *et al.*, Phys. Rev. D **66**, 010001 (2002).
15. C. Stratowa, R. Dobrozemsky, P. Weinzierl, Phys. Rev. D **18**, 3970 (1978).
16. J. Byrne, P.G. Dawber, M.G.D. van der Grinten, C.G. Habeck, F. Shaikh, J.A. Spain, R.D. Scott, C.A. Baker, K. Green, O. Zimmer, J. Phys. G **28**, 1325 (2002).
17. O. Zimmer, J. Byrne, M.G.D. van der Grinten, W. Heil, F. Glück, Nucl. Instrum. Methods A **440**, 548 (2000).
18. J.D. Jackson, *Classical Electrodynamics*, 3rd edition (Wiley & Sons, 1998).
19. T. Hsu, J.L. Hirshfield, Rev. Sci. Instrum. **47**, 236 (1976); G. Beamson, H.Q. Porter, D.W. Turner, J. Phys. E **13**, 64 (1980); P. Kruit, F.H. Read, J. Phys. E **16**, 313 (1983).
20. J. Byrne, J. Morse, K.F. Smith, F. Shaikh, K. Green, G.L. Greene, Phys. Lett. B **92**, 274 (1980).
21. V.M. Lobashev, P.E. Spivak, Nucl. Instrum. Methods A **240**, 305 (1985); V.M. Lobashev *et al.*, Nucl. Instrum. Methods A **238**, 496 (1985); V.M. Lobashev, V.N. Aseev, A.I. Belesev *et al.*, Phys. Lett. B **460**, 227 (1999).
22. H. Backe *et al.*, Phys. Scr. T **22**, 98 (1988); A. Picard, H. Backe, H. Barth, J. Bonn *et al.*, Nucl. Instrum. Methods B **63**, 345 (1992); C. Weinheimer, B. Degen, A. Bleile, J. Bonn, L. Bornschein, O. Kazachenko, A. Kovalik, E.W. Otten, Phys. Lett. B **460**, 219 (1999).
23. A. Osipowicz *et al.*, arXiv:hep-ex/0109033; C. Weinheimer, arXiv:hep-ex/0210050 v1.
24. D. Beck, F. Ames, M. Beck, G. Bollen, B. Delauré, J. Deutsch, J. Dilling, O. Foerstner, T. Phalet, R. Prieels, W. Quint, P. Schmidt, P. Schuurmans, N. Severijns, B. Vereecke, S. Versyck, Nucl. Phys. A **701**, 369c (2002).
25. S.R. Lee, P.G. Dawber, J. Byrne, *WEIN Conference Proceedings, Dubna, CIS* (JINR, Russia, 1992) p. 523.
26. J. Byrne, P.G. Dawber, S.R. Lee, Nucl. Instrum. Methods A **349**, 454 (1994).
27. T.G. Northrop, *The Adiabatic Motion of Charged Particles* (Interscience Publ., 1963).
28. P.C. Clemmow, J.P. Dougherty, *Electrodynamics of Particles and Plasmas* (Addison-Wesley Publ. Comp., 1969).
29. R. Dendy (Editor), *Plasma Physics: An Introductional Course* (Cambridge University Press, 1993).
30. F. Glück, Phys. Rev. D **47**, 2840 (1993).
31. H. Pietschmann, Acta Phys. Austriaca Suppl. (Particles, Currents, Symmetries), edited by P. Urban (Springer-Verlag, 1968) p. 88.
32. O. Nachtmann, Z. Phys. **215**, 505 (1968).
33. C.G. Habeck, doctoral thesis, University of Sussex (1997).
34. R. Dobrozemsky, Nucl. Instrum. Methods **118**, 1 (1974).
35. `www-cfadc.phy.ornl.gov` (go to: ELASTIC, Isotopomers of hydrogen ions ...).
36. P.S. Krstic, D.R. Schultz, J. Phys. B **32**, 2415 (1999); Phys. Rev. A **60**, 2118 (1999).
37. C.F. Giese, W.R. Gentry, Phys. Rev. A **10**, 2156 (1974); R. Schinke, Chem. Phys. **24**, 379 (1977); H. Krüger, R. Schrinke, J. Chem. Phys. **66**, 5087 (1977); G. Niedner *et al.*, J. Chem. Phys. **87**, 2685 (1987); D. Dhuicq, C. Benoit, J. Phys. B **24**, 3599 (1991).
38. R.K. Janev *et al.*, *Elementary Processes in Hydrogen-Helium Plasmas* (Springer-Verlag, 1987).
39. T. Tabata, T. Shirai, At. Data Nucl. Data Tables **76**, 1 (2000).
40. D.W. Koopman, Phys. Rev. **154**, 79 (1967); **166**, 57 (1968); M.W. Gealy, B. Van Zyl, Phys. Rev. A **36**, 3091 (1987); T. Kusakabe *et al.*, Phys. Rev. A **62**, 062714 (2000).
41. J. L'Ecuyer, J.A. Davies, N. Matsunami, Nucl. Instrum. Methods **160**, 337 (1979).
42. F. Glück, *Axisymmetric electric field calculation with charge density method*, to be published.
43. F. Glück, *Axisymmetric magnetic field calculation with Legendre polynomials and elliptic integrals*, to be published.
44. M.W. Garrett, J. Appl. Phys. **22**, 1091 (1951); see also in, *High Magnetic Fields*, edited by H. Kolm *et al.* (John Wiley & Sons, Inc., New York, 1962) p. 14.
45. G. Engeln-Müllges, F. Reutter, *Numerik-Algorithmen mit Fortran 77 Programmen* (Wissenschaftsverlag, 1993) Chapt. 17.
46. J.H. Verner, SIAM J. Numer. Anal. **15**, 772 (1978).
47. P.W. Hawkes, E. Kasper, *Principles of Electron Optics*, Vol. **1** (Academic Press, 1989).
48. E.R. Andrew *et al.*, J. Sci. Instrum. **43**, 936 (1966).
49. K. Kaminishi, S. Nawata, Rev. Sci. Instrum. **52**, 447 (1981).
50. F. Glück, *Axisymmetric coil design for homogeneous magnetic field*, to be published.